Journal Title
XX(X):2–27

DOI: 10.1177/ToBeAssigned
www.sagepub.com/
SAGE

Computational Characterization of the Secondary Droplets Formed During the Impingement of a Train of Ethanol Drops

David Markt Jr.[1], Ashish Pathak[1], Mehdi Raessi[1], Seong-Young Lee[2] and Roberto Torelli[3]

Abstract

This paper uniquely characterizes the secondary droplets formed during the impingement of a train of ethanol drops, using 3D direct numerical simulations performed under conditions studied experimentally by Yarin and Weiss (Journal of Fluid Mechanics, 1995). Our numerical results have been previously validated against experimental data demonstrating the ability to accurately capture the splashing dynamics. In this work, the predictive ability of the model is leveraged to gain further insight into secondary droplet formation. We present a robust post-processing algorithm, which scrutinizes the liquid volume fraction field in the Volume-of-Fluid method and quantifies the number, volume and velocity of secondary droplets. The high resolution computational simulations enable secondary droplet characterization within close proximity of the impingement point at small length and time scales, which is extremely challenging to achieve experimentally. By studying the temporal evolution of secondary droplet formation, direct connections are made between liquid structures seen in the simulation and the instantaneous distribution of secondary droplets, leading to detailed insights into the instability-driven breakup process of lamellae. Time-averaged secondary droplet characteristics are also studied to describe the global distribution of secondary droplets. Such analysis is vital to understanding fuel drop impingement in direct-injection engines, facilitating the development of highly accurate spray-wall interaction models for use in Lagrangian solvers.

Keywords

Secondary droplets, droplet impingement, spray-wall interaction

Introduction

The study of spray-wall interaction (SWI) is of critical importance to understanding fuel injection in modern internal combustion engines (ICEs). Under low chamber density and reduced engine speed conditions[1], when fuel spray is injected into the cylinder, fuel drops may impinge on the cylinder walls and piston head with two outcomes; deposition and splashing. It is known that deposited liquid fuel hinders efficient combustion, which leads to increased particulate matter and hydrocarbon emissions, especially during cold start conditions[2]. In Computational Fluid Dynamics (CFD) simulations of engines, fuel injection is commonly modeled in a Lagrangian framework, which requires the use of a SWI sub-model due to highly disparate length scales. Such models predict the onset of splashing, the amount of splashed liquid mass, and the number, size and velocity of secondary droplets. Due to the difficulty in characterizing secondary droplets formed during the chaotic spray impingement process, single drop impingement is often studied to generate SWI models. Many studies of single drop impingement onto dry and wetted surfaces have been conducted and are summarized by Moreira et al.[3], Yarin[4] and Liang and Mudawar[5]. Much work has been done to characterize the onset of splashing during such single drop impingements, while the formation and distribution of secondary droplets is less understood.

Some common models used to predict secondary droplet distributions are those of Bai et al.[6], Mundo et al.[7], O'Rourke and Amsden[8] and Roisman et al.[9], which are based on data from single drop impingements. Although such models are widely used in Lagrangian solvers, it has been found that single drop impingement models cannot accurately predict the splashing phenomena of dense sprays[3,5]. In Markt et al.[10], simulations of the impingement of diesel drop trains under engine relevant conditions were performed. It was shown that the common SWI model of O'Rourke and Amsden[8] over predicts the amount of splashing under such impingement conditions. This suggests ICE relevant impingement characteristics (drop size and velocity) and the influence of subsequent drops must be taken into

[1]University of Massachusetts - Dartmouth
[2]Michigan Technological University
[3]Argonne National Laboratory

Corresponding author:
Mehdi Raessi, University of Massachusetts - Dartmouth
Dartmouth, Ma, United States
Associate Professor
Email: mraessi@umassd.edu

Prepared using sagej.cls

consideration to be able to accurately predict the splashing phenomena. These findings demonstrated the need for SWI models which consider the interaction of multiple impinging drops.

Although a train of mono-dispersed drops is an idealized representation of a fuel spray, it has yielded more accurate predictions of fuel impingement than single drop models. The following studies have focused on the impingement of mono-dispersed drop trains. In Yarin and Weiss[11], experiments and theory were used to study the impingement of drops composed of ethanol or an ethanol-water-glycerol mixture onto a stainless steel surface. The splashed liquid mass, number and size of secondary droplets were characterized for many impingement cases. The splashing criterion developed by Yarin and Weiss[11] uses impingement frequency to account for multidrop interactions. Following the experiments of Yarin and Weiss[11], Markt et al.[12] studied the surface impingement of single ethanol drop trains using highly resolved 3D simulations, in which global features were quantified (e.g., transition to splashing, splashed mass ratio and composition of splashed mass). Mundo et al.[13] performed experiments to investigate the impingement of drops composed of water, ethanol or a water-sucrose-ethanol mixture onto a rotating stainless steel disc. From the experiments, distributions of secondary droplet diameter and velocity were quantified for many impingement conditions. In the work of Samenfink et al.[14], the impingement of a train of drops on a shear-driven liquid film was studied. The splashed mass, secondary droplet size, velocity and angle were reported[14]. Richter et al.[15] analyzed the influence of surface temperature and impingement frequency on secondary droplet size and formation.

Building upon experimental studies,[11,13] Stanton and Rutland[16] developed a SWI model which combined the impingement-frequency-based splashing threshold of Yarin and Weiss[11] and the secondary droplet distributions of Mundo et al.[13]. This SWI model was implemented into the KIVA-II code and was found to improve the agreement with the experimental data in terms of global spray quantities such as the deposited liquid mass[16]. However, local quantities such as secondary droplet velocity and diameter showed discrepancies when compared to the experimental results. This suggests that using single drop trains to model dense sprays has limitations, as they are unable to fully capture the complex surface impingement dynamics. Extending upon single drop trains, Cosalli et al.[17] performed experiments in which arrays of drops impinged within close proximity to one another. Although arrays of drops are still a simplified representation of spray, new splashing dynamics not present during single drop and single train impingement were observed. At drop-to-drop interaction sites liquid jets were formed leading to increased splashing. Furthermore, splashing was found to occur below the threshold prediction for single drop impingements[17]. While studies such as this are helpful in understanding the interactions between neighboring drops, the real spray impingement phenomenon involves drops of various size and velocity which impinge within close proximity. To provide insight into the chaotic spray impingement process

without simplification, Sivakumar and Tropea[18] and Roisman and Tropea[19] performed experiments with water sprays. Both studies determined that fluctuations in film thickness and film velocity alter the splashing dynamics, concluding that the superposition of single drop impingements does not provide accurate splashing predictions. Despite such efforts, several spray impingement processes, including interaction of multiple drops, are still not fully understood.

Even with their simplification, studies of single drop trains can still assist in bridging the knowledge gap between single drop and complex spray impingement by better understanding the splashing dynamics and secondary droplet formation which arise from the interaction of subsequent impingements. Therefore, the current computational study focuses on the characterization of the secondary droplets formed during the splashing of drop trains[11]. A robust algorithm was developed to characterize secondary droplets and obtain drop size, velocity and velocity angle with respect to the surface. The temporal evolution of the secondary droplet distribution is presented for short time scales near the impingement point, providing details of the secondary droplet formation process. Furthermore, time averaged secondary droplet distributions are reported for three impingement frequencies. The secondary droplet characterizations provided here can be useful for SWI model development, and the methodology developed may be extended to study the chaotic phenomenon of fuel spray impingement.

Numerical Methods

Multiphase Flow Solver

In the current study, an in-house multiphase flow solver[20] is used, which solves the full Navier-Stokes equations for an incompressible immiscible flow in a fully Eulerian framework. With such assumptions, the conservation of mass and momentum, equations 1 and 2, respectively, are solved numerically

$$\nabla \cdot \vec{U} = 0 \tag{1}$$

$$\frac{\partial}{\partial t}\left(\rho\vec{U}\right) + \nabla \cdot \left(\rho\vec{U}\vec{U}\right) = -\nabla P + \nabla \cdot \tau + \vec{F}_B + \vec{F}_{ST} \tag{2}$$

using the mass conserving Volume-of-Fluid (VOF) method to track the phase volumes, i.e., liquid and gas, in a sharp manner[21]. The fluid volumes are tracked using a scalar function, α, which is defined to be unity in the liquid and zero outside. To track the fluid throughout the domain, the following transport equation is solved

$$\frac{\partial \alpha}{\partial t} + \vec{U} \cdot \nabla \alpha = 0 \tag{3}$$

using the geometric approach of Youngs[22]. This approach employs Piecewise Linear Interface Calculation (PLIC), where the interface is represented by a planar polygon in each computational cell. The equations are discretized following the finite volume method, and are solved using the two-step projection method[20, 23]. To prevent artificial deformation of the phase interfaces in high density ratio multiphase flows, a consistent scheme is used to perform mass and momentum transport[24]. The surface tension force is implemented numerically following the balanced-force algorithm[25], where the pressure discretely balances the surface tension force, reducing spurious currents. The flow solver employs a MPI parallel framework which has shown great scalability[26]. Recently, a fast multigrid preconditioned pressure Poisson solver was developed, which was shown to significantly accelerate the simulations[27]. A full description of the governing equations and numerical details can be found in Pathak and Raessi[20]. The flow solver has been extensively validated in previous studies[21, 20, 27]. Recently, the solver was used to simulate the surface impingement of a train of fuel drops, and was found to accurately capture the splashing dynamics of fuel drops[10, 12]. In Markt et al.[12], a multiple passive scalar routine was implemented, providing the capability to passively tag different portions of the same liquid. The routine tags each droplet with a distinct scalar function, c_n, advected by the following transport equation

$$\frac{\partial c_n}{\partial t} + \vec{U} \cdot \nabla (c_n) = 0 \tag{4}$$

which is solved using the same geometric VOF method[12, 21]. Passive scalars are used in the current study, providing detailed insight into the splashing process, which is not possible experimentally.

Drop Train Impingement Simulations

All ethanol drop train impingement simulations presented in the current work were performed in a quarter domain to reduce the computational cost of the problem. However, the impingement dynamics are allowed to develop naturally within the quarter domain, and no constraints on symmetry are enforced with respect to lamella and secondary droplet formation. Therefore, the imposed quarter domain symmetry is not expected to significantly alter the impingement dynamics of the drop train. All simulations were performed with a resolution of 80 cells per diameter (CPD) of the drop, corresponding to a spatial resolution of 1.375μm. This resolution was found to be sufficient to accurately capture lamella breakup and secondary droplet formation[12]. In Markt et al.[12], ethanol drop train impingement simulations were performed under similar impingement conditions. It was determined that a resolution of 80 CPD was able to capture the breakup of lamellae and match the experimental splashed mass ratio of Yarin and

Weiss[11] well. That provided confidence that the majority of secondary droplets would be fully resolved. A comparison of the secondary droplet distributions from simulations at 40 and 80 CPD are presented later in the results section, which establishes further confidence in the accuracy of the results obtained from simulations at 80 CPD.

Secondary Droplet Characterization Algorithm

To identify and characterize secondary droplets within the 3D numerical domain, a robust post-processing algorithm was developed. The algorithm identifies isolated liquid structures defined by a scalar field, and characterizes their number, size and other quantities of interest, e.g., velocity. Designed for simulations performed using the VOF method, the liquid volume fraction field is scrutinized within an area of interest to identify isolated portions of liquid. We will refer to isolated liquid structures as "droplets" for ease of presentation, although the liquid structures are not necessarily spherical forming a droplet. The secondary droplet characterization algorithm is detailed next.

Suppose computational cells within the control volume of interest range from $i = 1 \rightarrow N_x$, $j = 1 \rightarrow N_y$ and $k = 1 \rightarrow N_z$ where N_x, N_y and N_z are the total number of cells in the x, y and z directions, respectively. Distinguishing individual droplets is achieved through a droplet tagging methodology. The volume fraction in each cell of the control volume is analyzed using nested for loops; starting at cell $i = 1$, $j = 1$, $k = 1$, and moving to $i = N_x$, $j = N_y$ and $k = N_z$, respectively. When a cell is found to contain liquid (volume fraction greater than zero), it is tagged with the most current droplet number. The volume fraction in the $i + 1$ neighboring cell is then measured. If the neighboring cell also contains liquid, the droplet interface has not yet been located and the droplet number remains the same. If the neighboring cell does not contain liquid, the droplet interface has been located and the droplet number is incremented. This ensures the next secondary droplet will be tagged with a new droplet number. The droplet number is also incremented at the control volume boundary where there are no neighboring $i + 1$ cells. During the initial droplet numbering phase, each cell is also flagged to identify cells which are located on control volume boundaries. The cells are given a boundary condition flag (BC flag) as follows:

$$\text{BC flag} = \begin{cases} 0; & \text{Internal cell or closed boundary} \\ 1; & \text{Single symmetry boundary} \\ 2; & \text{Two symmetry boundaries} \\ 3; & \text{Open boundary} \end{cases}$$

This flagging is performed to ensure secondary droplets are correctly accounted for. Simulations performed in a full domain acquire the following BC flags: secondary droplets in the interior of the

control volume, or on a closed boundary (BC flag = 0), are counted only once. Any droplet in contact with an open boundary (BC flag = 3) is either leaving or entering the control volume, and has a compromised volume, therefore such droplets are not counted. It is not that such droplets are never counted; it is only during the instant when they are entering or leaving the control volume that they are not counted. This is done to ensure the accuracy of the secondary droplet diameter, as such droplets would be characterized as smaller than their actual size. In simulations that exploit the symmetry of the problem and, for example, are performed in a quarter domain, we must count droplets differently. Any secondary droplet within the interior of the domain (BC flag = 0) is counted four times. A droplet which is in contact with a symmetry boundary (BC flag = 1) will have its volume doubled and is only counted twice. Droplets in contact with two symmetry boundaries (BC flag = 2), have their volume multiplied by four and are counted only once. Finally, as with the full-domain, any droplets on open boundaries (entering or leaving the control volume) are not counted due to their compromised volume.

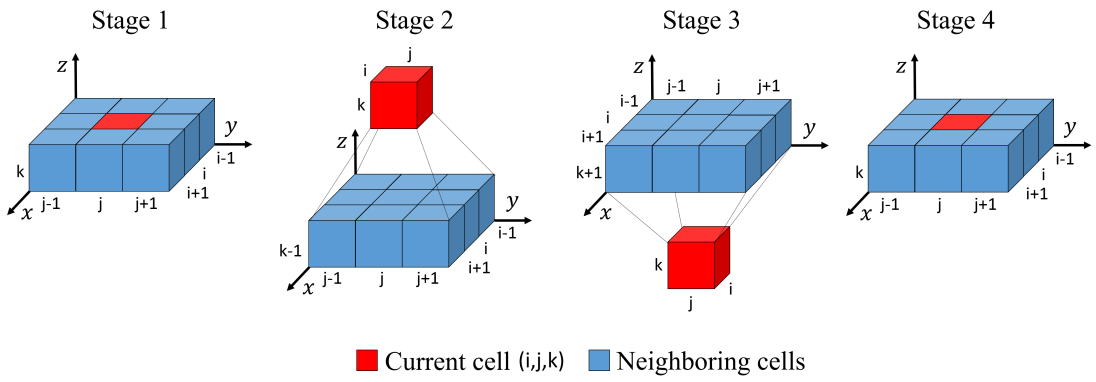

Figure 1. The four stages used to condense the droplet number within each secondary droplet. Droplet number information is shared from the neighboring cells (blue) to the current cell (red) to ensure all connected liquid filled cells have the same droplet number.

After the initial droplet numbering phase, each cell in the control volume has been assigned a boundary condition flag, and any cell containing liquid is tagged with a droplet number. At this point, cells which compose the same secondary droplet will have different droplet numbers, as the initial droplet numbering phase only checks the $i+1$ neighboring cell to locate the droplet interface and increment the droplet number. To condense the droplet number within each secondary droplet and ensure every cell has the same droplet number, a series of four condensing stages are used. As seen in Figure 1, the droplet number information is shared between neighboring cells (blue to red) in each condensing stage.

Here only cases for cells which are in the interior of the control volume are shown. Cells which are on one or more control volume boundaries share droplet number information between as little as seven neighboring cells. In stages 1 and 4, the droplet number information in condensed in each xy plane. In stages 2 and 3, the droplet number information is compared to the 9 neighboring cells in the $k-1$ and $k+1$ xy planes, respectively. Condensing droplet numbers in the current xy plane is performed twice (stages 1 and 4) to ensure cells on droplet interfaces obtain the correct droplet number. If not performed twice, some interfacial cells for droplets with high curvature do not obtain the correct droplet number. Although compared with neighboring cells in stages 1-3, it is not until stage 3 that the neighboring cells themselves obtain the correct droplet number. Therefore, an additional phase is necessary to properly number the interfacial cells in such scenarios. The pseudocode for the droplet number condensing algorithm is shown below, where the neighboring cells changes for each stage. Note the second for loop represents the nested for loops in the i, j and k directions, respectively, and is represented as one loop for the sake of brevity.

for Stages 1 to 4 **do**
  for $k = 1$ to N_z, $j = 1$ to N_y, $i = 1$ to N_x **do**
    Compare droplet number(i,j,k) to neighboring droplet numbers. (Neighbors depend on which stage of condensing is being performed: Figure 1)
    if droplet number(i,j,k) $>$ neighboring droplet number **then**
      droplet number(i,j,k) = neighboring droplet number
    end if
  end for
end for

Once the droplet numbers have been condensed, the number of distinct droplets is counted. The volume fractions of all cells which compose a secondary droplet are then summed to determine the "total volume fraction" of the secondary droplet. The total volume fraction is then multiplied by the volume of a cell ($\Delta x \times \Delta y \times \Delta z$), which is uniform, to determine the droplet volume. Most secondary droplets are not spherical and therefore do not have a simple way to characterize their diameter without knowing information about the interface orientation (e.g., Sauter Mean Diameter). Thus using the droplet volume, the equivalent diameter of a spherical droplet with the same volume is calculated as an approximation. The velocity components and magnitude are also calculated for each droplet. To yield accurate droplet velocities, the velocities in interfacial cells are excluded to avoid introducing the gas velocity. The velocity of all internal cells within the droplet are averaged to determine the droplet velocity. Each

droplet then acquires the largest boundary condition flag of any of the cells which comprise it, since as the boundary condition flag increases in number, the droplet is counted a lesser number of times.

Results

Droplet Characterization Validation

Many tests were performed to assess the accuracy of the secondary droplet characterization algorithm and demonstrate its robustness. Here we will present only one for the sake of brevity. Figure 2 shows a sample test that includes a set of liquid structures with prescribed volume fractions as follows: a droplet with an irrational diameter, two droplets separated by one computational cell, two droplets connected by one computational cell, four under resolved droplets and an angled truncated cylinder (representing ligaments formed during drop impingement). Each geometry had a different velocity prescribed to the interior cells, while all geometries had the same velocity applied to interfacial cells, making it possible to ensure the interfacial cells were not used in the droplet velocity calculation. Comparing the results with the known prescribed values, the algorithm was found to capture the exact number of droplets, droplet volume, diameter (where applicable) and velocity, demonstrating the robustness of the algorithm for complex geometries.

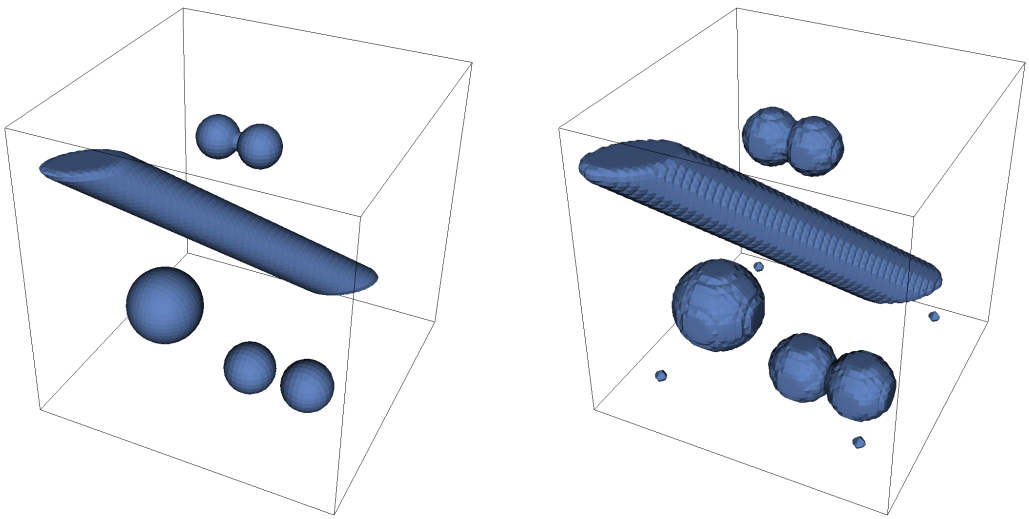

Figure 2. A sample test case used to validate the secondary droplet characterization algorithm: (a) visualized with an isovolume of 0.5 (regular visualization). (b) Visualized with an isovolume of 0.01 to capture the four under resolved droplets used to test the algorithm.

Splashing: Stages of Secondary Droplet Formation

The simulations presented here follow the experimental work of Yarin and Weiss[11], where a train of ethanol drops impinges on an initially dry stainless steel surface. Three impingement frequencies were studied in the current work, all with a droplet diameter D = 109μm and an impingement velocity V_0 = 10m/s. The ethanol properties are ρ = 800kg/m^3, σ = 22.8$\times10^{-3}$ N/m and ν = 1.4975$\times10^{-6}$m^2/s and the air properties are ρ = 1.226kg/m^3 and ν = 1.45$\times10^{-5}$m^2/s. To ensure splashing would occur, the impingement conditions were selected to provide nondimensional velocities, u, defined in Eq. 5, above the experimentally determined splashing threshold u = 16-18[11].

$$u = \frac{V_0}{(\sigma/\rho)^{1/4}\nu^{1/8}f^{3/8}} \tag{5}$$

The impingement frequency, f, was the only parameter varied to achieve nondimensional velocities of u = 19, 22 and 25. Therefore, the Weber and Reynolds numbers at impact are 382 and 7279, respectively, and are the same for all cases. In Yarin and Weiss[11], no contact angle was reported due to its negligible role in the short, transient film formation period. In our previous work[12], ethanol drop train simulations were performed over a wide range of u under the same impingement conditions as the current study; a 90^o constant contact angle was used, which was found to have no adverse effects on the splashing threshold or splashed liquid mass[12]; therefore the same contact angle was used in the current study. The domain size, expressed in droplet diameters is 3.23$D\times$3.23$D\times$2.83D and was selected based on preliminary simulations[12] to ensure all secondary droplets are captured. To allow secondary droplets to leave the domain after being characterized, all domain boundaries are open to flow except the bottom wall (impingement surface) and two symmetry walls. Each drop is initialized at (0,0,2.26D) with a downward velocity (V_0) at appropriate times to achieve the desired impingement frequency. All figures showing simulation results are visualized with an isovolume of 0.5 for the VoF scalar field.

To highlight the unparalleled capabilities provided by the passive scalar routine, selected results from the simulation at u = 22 (f = 11.50 kHz) are presented in Figure 3. The results are shown at different dimensionless times, T, defined as T = tf, where t is the physical time and T = 0 corresponds to the impingement of the first drop in the drop train. Dimensionless time is used to allow for comparison between simulations with different impingement frequencies. For all simulations a dimensionless time, (n), will correspond to the impingement of the ($n+1$) drop in the drop train. Note three repeating colors are used to tag the impinging drops in all simulations: yellow, red, and green.

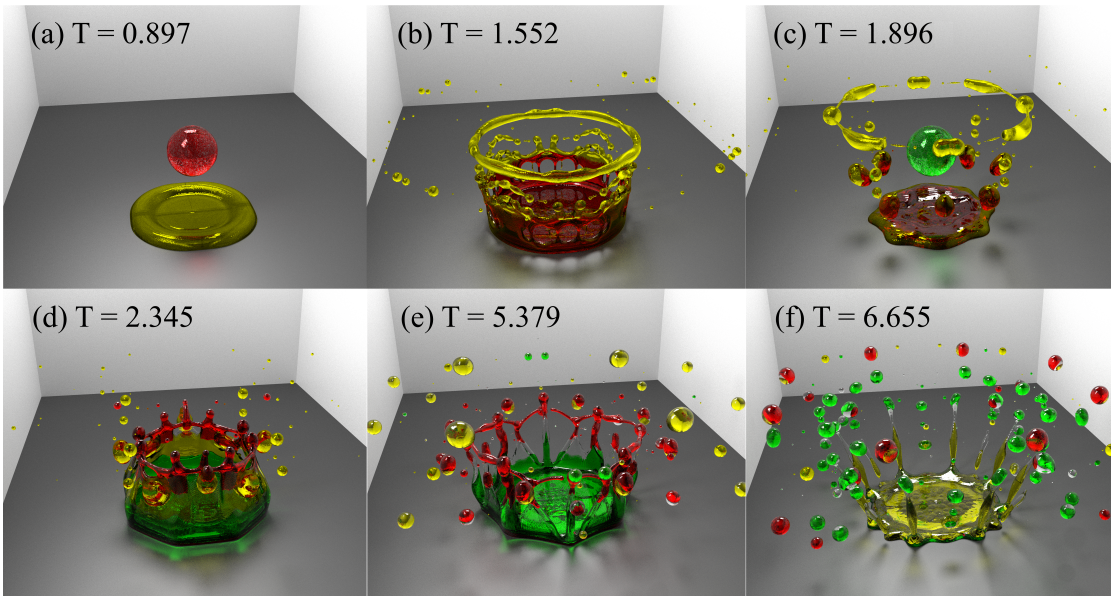

Figure 3. Results from the ethanol drop train impingement simulation at u = 22 at different dimensionless times. The first, second and third drops in the drop train shown in (a-d) are colored yellow, red and green respectively. (e and f) Lamella fracturing and secondary droplet ejection are shown after the impingement of the sixth (green) and seventh (yellow) drops, respectively.

In Figure 3(a), the first drop in the drop train (yellow) has impinged and is receding while the second drop (red) is nearing impingement. The second drop has impinged in Figure 3(b), forming an unstable lamella from which secondary droplets pinch off or eject before fracturing. Figure 3(c) shows the fracturing of the unstable lamella from the second drop impingement. Note the secondary droplets are mostly composed of the film established by the first drop (yellow), while only a small portion of the secondary droplets are composed of the second drop (red). At this time, the third drop (green) is moving towards the liquid film. After the impingement of the third drop in Figure 3(d), a lamella and cusps form which are composed of the liquid from all three drops. This lamella will eventually eject secondary droplets which are composed of all three drops. In Figure 3(e), after the impingement of the sixth drop (green) a fracturing lamella is seen, composed of drops five (red) and six. The cusps at the top of the lamella are beginning to eject secondary droplets composed of the fifth drop, while secondary drops from the fourth drop (yellow) can still be seen in the domain. Finally, in Figure 3(f), after the impingement of the seventh drop (yellow), ligaments form after the lamella fractures, extending from the film to the cusps. The ligaments eventually break up into secondary droplets. As seen in Figure

3, the passive scalar routine provides the ability to track the liquid from each drop as it is splashed, yielding information on the composition of the secondary droplets. Such analysis is nearly unobtainable experimentally, as diffusive effects may compromise the ability to sharply track the liquid from each drop of the drop train. This information is necessary for Lagrangian solvers. Currently those solvers consider secondary droplets solely composed of the impinging drop; but here we see that the secondary droplets are mainly composed of the already accumulated liquid film. Although the impinging drop and the film are composed of the same liquid, their properties may significantly differ. Under engine-like conditions, heat transfer between the liquid film and piston may change the thermo-physical properties of the film. Therefore, it is important to identify the composition of splashed mass to correctly assign liquid properties and improve predictability of the evaporation of secondary droplets.

All drop train impingement simulations performed in the current work exhibit splashing, where lamella instability leads to cusp formation and secondary droplet ejection, consistent with the splashing definition and threshold of Yarin and Weiss[11]. In all simulations, splashing occurs after the impingement of the second, and all subsequent drops. In Figure 4(a-c), lamella instability and secondary droplet formation are shown for the drop train impingements at u = 19 (f = 16.92 kHz), 22 (f = 11.50 kHz) and 25 (f = 8.14 kHz), respectively.

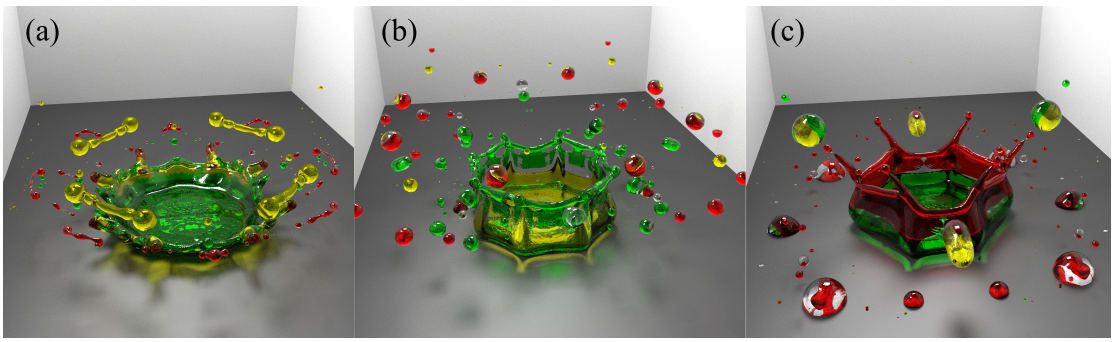

Figure 4. Results from the ethanol drop train impingement simulations at (a) u = 19, T = 2.588 (b) u = 22, T = 6.276 (c) u = 25, T = 8.202. The dimensionless times were selected only to highlight exemplary lamella formation. In all simulations lamella instability leads to secondary droplet ejection, classifying the impingement outcome as splashing.

Focusing on the impingement at u = 22, three distinct phases of secondary droplet ejection are seen. In Figure 5, the sixth drop (green) has just impinged and the unstable lamella ejects secondary droplets. Figures 5(a-c) are at dimensionless times of T = 5.172, 5.517 and 5.862, respectively, showing multiple

stages of droplet ejection during the impingement of the same drop. In each image, an example of the secondary droplet ejection is circled in black. The lamella instability in Figure 5(a) causes the first phase of secondary droplet formation, where small droplets are ejected from the cusps. As the lamella fractures in Figure 5(b), ligaments are formed which eject large secondary droplets from jets at the top of the ligaments, marking the second phase of droplet ejection. Finally, in Figure 5(c) the third phase of secondary droplet ejection is present, where the ligaments break up into multiple secondary droplets of varying sizes. At this time the seventh impinging drop (yellow) is seen in the domain, moving towards the liquid film before impingement. Using the passive scalars, additional insight into the impingement process is gained. With this unique capability, it was determined the secondary droplets formed in the first two phases of droplet ejection are composed of the previously impinged drop or the film liquid, and not of the impinging drop. A more detailed description of the drop train impingement process and the splashed mass composition can be found in Markt et al.[12], where it was determined that at pseudo-steady state 93% of the splashed liquid mass during each impingement is composed of the previously impinged drop. Consistent with this finding, the droplets in Figure 5(a) and (b) are composed of the fifth impinged drop (red), not the currently impinging sixth drop (green). The ligaments seen in Figure 5(b) are composed of both the red and green drop liquid. The upper portion of the ligament is red while the lower portion is composed of the green drop which has just impinged. It is not until the third stage of secondary droplet formation that the liquid from the impinging drop is splashed.

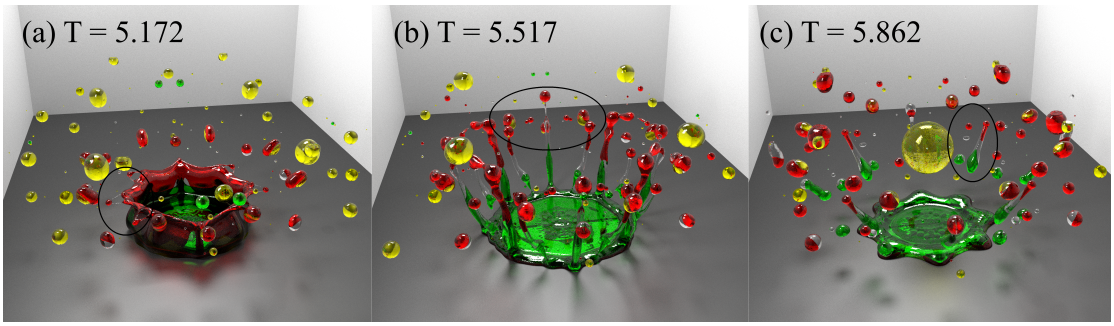

Figure 5. Results from the ethanol drop train impingement at u = 22 for three dimensionless times. (a) First phase of secondary droplet ejection where small droplets are ejected from lamella cusps. (b) Second phase of droplet ejection after the formation of ligaments at cusp locations. Larger secondary droplets are ejected from jets at the top of the ligaments. (c) Third phase of droplet ejection when the ligaments fracture into droplets of many sizes. Note the large yellow drop is the seventh drop of the drop train moving towards the surface before impinging.

Temporal Evolution of Secondary Droplets

We will now present the temporal evolution of secondary droplets for the impingement at u = 22. In the current post-processing, liquid is considered splashed only after impinging and crossing a "splashing threshold height", which is used to distinguish between deposited and splashed liquid mass at any time during the impingement process. The splashing threshold height used in the current study is 70μm, and was taken from Markt et al.[12]. It was also shown that the use of the splashing threshold height does not alter the calculation of splashed liquid mass, or secondary droplets[12]. Therefore the "splashed control volume", in which the secondary droplets are quantified, is the full numerical domain above the splashing threshold height (70μm).

Quantitative details of secondary droplet formation are acquired by characterizing the temporal evolution of secondary droplets throughout the impingement process. In Figure 6, the number of secondary droplets and the percent of total secondary droplet volume, which is currently in the domain, are shown at dimensionless times T = 5.172, 5.517 and 5.862 for u = 22. Note the dimensionless times correspond with the images shown in Figure 5(a-c), respectively. The results are shown in terms of dimensionless diameter, d/D, where d is the secondary droplet diameter. The bin size of the histograms is Δx, or, D/80. At T = 5.172, there are many small secondary droplets in the range d/D = 0.0063-0.044, which are composed of the droplets from the first phase of droplet ejection, shown in Figure 5(a), and from the previously impinged fifth droplet (yellow). Although the majority of droplets are within this size range, they represent a negligible portion of the total secondary droplet volume. The majority of the secondary droplet volume is represented by 30 droplets in the size ranges d/D = 0.24-0.27, 0.33, 0.42 and 0.51. The large droplets at this time (d/D = 0.33, 0.42 and 0.51) are due to the unfractured lamella rim. At this time, the lamella rim is mostly intact and is characterized as large secondary droplets. A short time later at T = 5.517, the number of small secondary droplets (d/D = 0.0064-0.044) has decreased due to the secondary droplets from the previous impingement leaving the domain. At the same time an increase in the number of droplets of size d/D = 0.1-0.45 is caused by the droplets ejected from the ligaments (second droplet ejection phase), shown in Figure 5(b). With the lamella now fractured into ligaments, the majority of the secondary droplet volume is no longer represented by the lamella rim, but instead by droplets of size d/D = 0.25-0.45. Finally, after the third phase of droplet ejection at T = 5.862, an increase in the number of small secondary droplets is seen. Here the maximum number of secondary droplets is present due to ligament breakup, with 238 secondary droplets currently in the domain. An increase in the secondary droplets of size d/D = 0.15-0.4 is also seen which represents the majority of the secondary droplet volume. More specifically, 66% of the secondary droplet volume is represented by 24 droplets, with 8 droplets of sizes d/D = 0.26, 0.33 and 0.37.

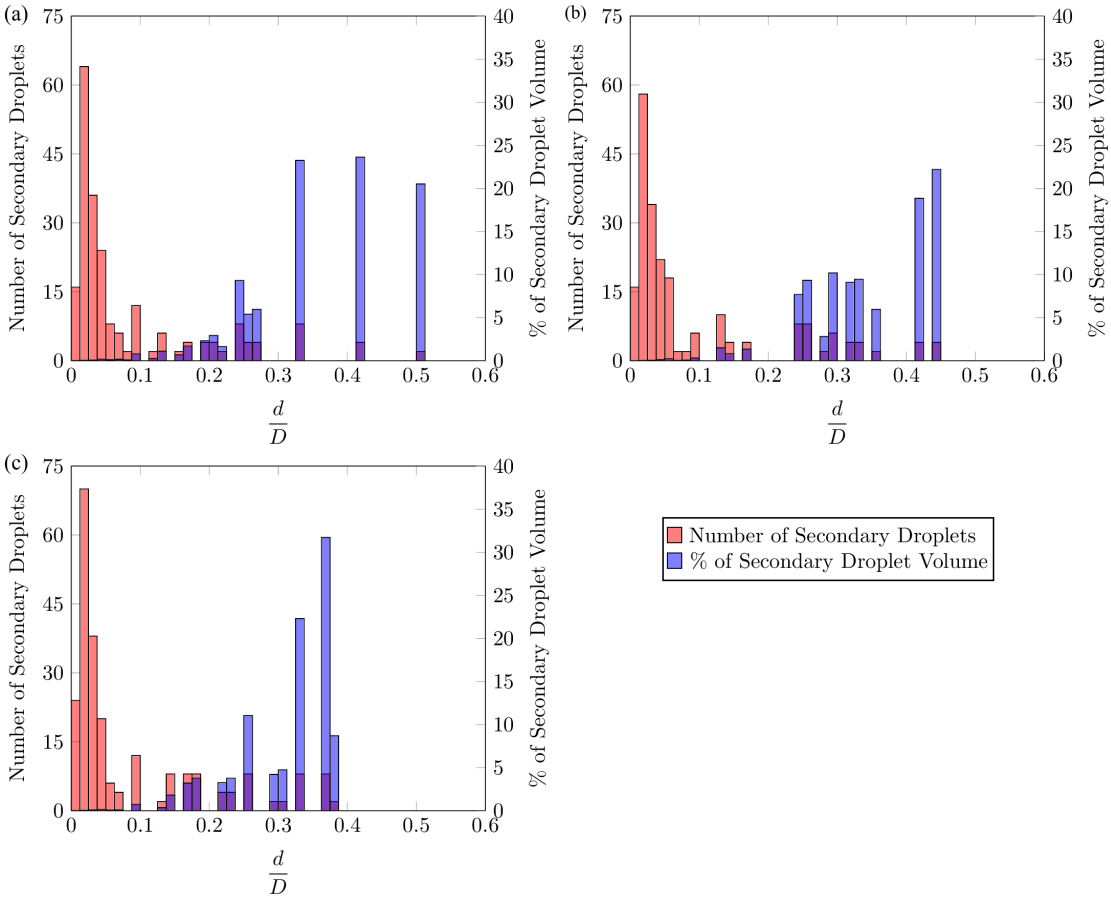

Figure 6. Temporal variation of the number of secondary droplets and percent of total secondary droplet volume as a function of dimensionless diameter, d/D, for the drop train impingement at u = 22. Dimensionless times of (a) T = 5.172, (b) 5.517 and (c) 5.862 correspond to the results shown in Figure 5(a-c), respectively.

Secondary Droplet Variation: Drop-to-drop Comparison

Instantaneous secondary droplet distributions were also quantified for the impingement of specific drops within the drop train. In the previous section, the instantaneous secondary droplet distributions were presented within a short time scale for the impingement of a single drop (drop 6 in the drop train), providing details on the phases of secondary droplet formation. In contrast, the following analysis shows the variation of secondary droplets produced from subsequent impingements. Secondary droplet distributions are presented for the impingement of drops 3 to 8 for the simulation at u = 22. Results are shown in Figure 7 at the same dimensionless time (T) after each impingement to directly compare the

splashing dynamics of each subsequent impingement. The distributions correspond to times after final stage of secondary droplet formation (ligament breakup) for each drop. From a qualitative comparison the similarity in secondary droplets at T = 4.9, 5.9, 6.9 and 7.9 is readily apparent. In Figure 7(c-f), a large number of small and medium sized secondary droplets are seen in the domain with similar spatial distribution and apparent velocity angle. This is in contrast to Figure 7(a) and (b), in which a smaller number of large secondary droplets are seen with a much different spatial distribution. Here the secondary droplets are concentrated above the impingement point suggesting the velocity angle with respect to the surface is much greater. Larger drops are also seen in Figure 7(a) and (b) due to coalescence of drops from the previous impingements. The results presented in Figure 7 suggest the impingement dynamics may be considered pseudo-steady state after the impingement of the fifth drop (T = 4.9) in the drop train. Differences in the instantaneous film momentum at the time of impingement and interaction with previously formed secondary droplets may cause slight differences in local secondary droplet numbers. Although the exact number of secondary droplets may be different, the same size droplets are expected once pseudo-steady state dynamics are present.

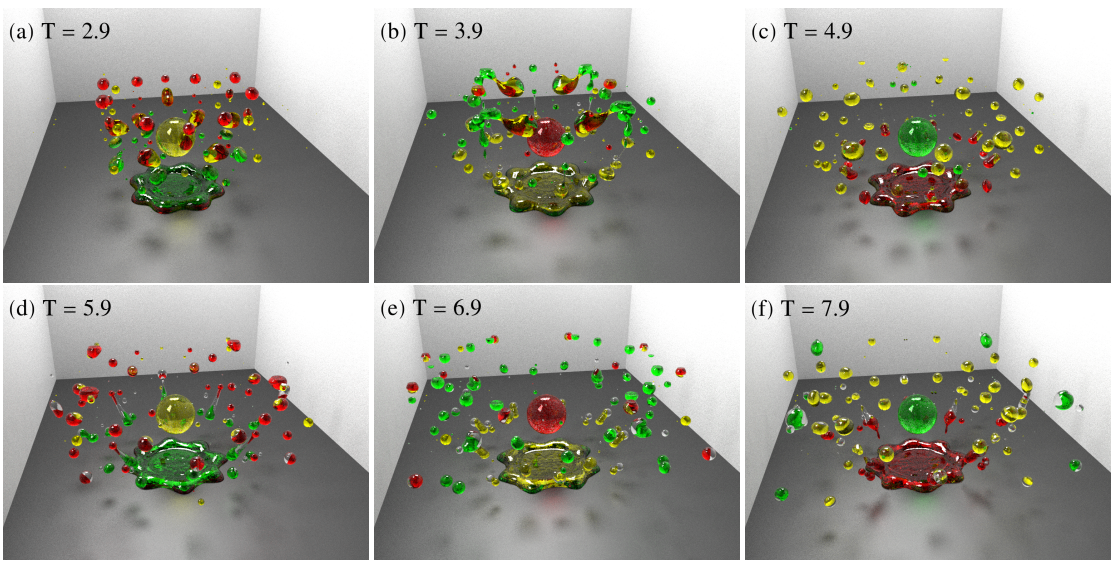

Figure 7. Simulation results for the ethanol drop train impingement case at u = 22. Results are shown after the impingement of the third through eight drops respectively. Note the similarity in secondary droplet distributions in (c-f), which indicate pseudo-steady state dynamics have been reached, while in (a) and (b) the early transient impingement dynamics are present resulting in a different secondary droplet distribution.

To quantitatively confirm pseudo-steady state splashing dynamics are present, the instantaneous secondary droplet distributions are compared as shown in Figures 8(a-f) at the same dimensionless times as Figure 7(a-f). Comparing the distributions in Figures 8(c-f), which correspond to drops 5 to 8, similarities in the representation of secondary droplet volume are seen. For these four impingements, the majority of secondary droplet volume is comprised of droplets of diameter $d/D \approx 0.25$, 0.31 and 0.4. The distributions from drops 5 and 7 (Figures 8(c) and (e)) have nearly identical secondary droplet distributions showing the consistency of the impingement dynamics. The secondary droplets formed from the sixth and eighth drop impingement (Figures 8(d) and (f)) have slightly different distributions. In Figure 8(d), a large portion of the secondary droplet volume is of size $d/D = 0.31$. This is due to a greater number of drops formed from the third stage of droplet formation, ligament breakup, which is also evident in Figure 7(d), as large elongated drops, formed from the ligament breakup, are seen. A similar phenomenon is observed from the impingement of the eighth drop. Although these ligament structures slightly alter the exact distribution of secondary droplets, impingements 5 to 8 yield the same size ranges of secondary droplets. The difference between the transient and pseudo-steady state splashing dynamics is clear when comparing the distributions from drops 5 to 8 with drops 3 and 4. When comparing the secondary droplet distributions in Figure 8(a) and (b), no clear trend is seen. The impingement of the third drop produces a wide range of secondary droplets and large drops which are not seen in the pseudo-steady state impingement. After the impingement of the fourth drop (Figure 7(b)) there is a narrower range of secondary droplets with a large portion of the mass represented by quite large drops as seen in Figure 8(b). The large drops are due to coalescence of drops from previous impingements, a phenomenon which is not seen during the pseudo-steady state impingements. The qualitative and quantitative analyses, presented in Figures 7 and 8, show the distinction between transient and pseudo-steady state secondary droplet formation.

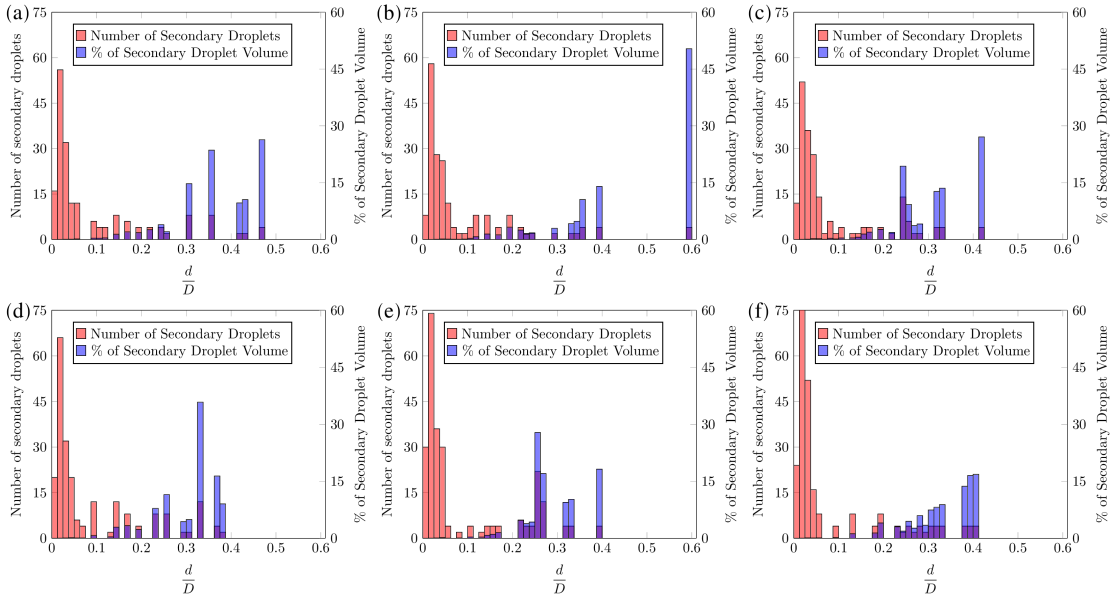

Figure 8. Instantaneous secondary droplet distributions from the ethanol drop train simulation at u = 22. Distributions are presented at dimensionless times of: (a) T = 2.9 (b) T = 3.9 (c) T = 4.9 (d) T = 5.9 (e) T = 6.9 (f) T = 7.9 corresponding to the simulation results presented in Figure 7(a-f).

Effects of Grid Resolution and Bin Size on Secondary Droplets

To assess the effect of grid resolution on the formation of secondary droplets, a drop train impingement simulation at u = 22 was performed at 40 CPD. A 160 CPD simulation was not performed due to its significantly high runtime, hence a proper grid convergence analysis was not possible. The secondary droplet distributions from both the 40 and 80 CPD simulations are shown in Figure 9, with two bin sizes to provide insight into the effects of bin size on the secondary droplet distribution.

In both simulations, the distribution secondary droplet volume (Figure 9(b) and (d)) is quite similar, showing only a slight dependence on grid resolution. As the bin size is reduced, peaks in the percent secondary droplet volume become more clear and distinct. When comparing the number of secondary droplets (Figure 9(a) and (c)), the simulation at 40 CPD contains fewer secondary droplets in the size range of d/D = 0.0125-0.0375. Although a smaller number of secondary droplets is observed, the trend in the number of secondary droplets is the same in both simulations. The majority of secondary droplets are of size $d/D < 0.0631$ with much fewer large drops up to size $d/D \approx 0.6$. The similarity of the distributions in Figures 9(a) and (c) show that the number of secondary droplets is not significantly affected by bin

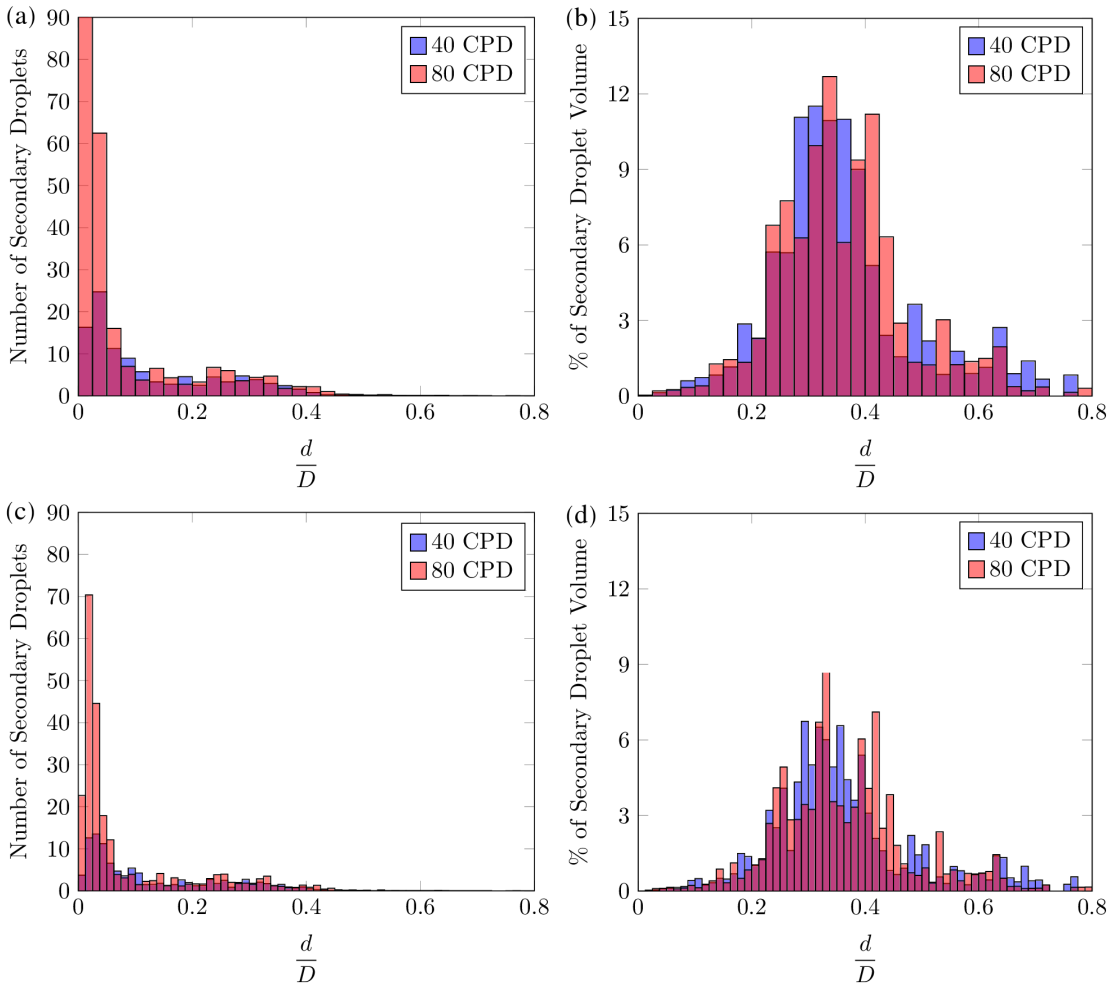

Figure 9. Secondary droplet distributions for the drop train impingement at u = 22 with a bin size of 2.75 μm (top row) and a bin size of 1.375 μm (bottom row).

size. This analysis provides confidence that the small secondary droplets are not formed due to numerical diffusion. Although a complete convergence analysis was not performed, the results show a trend towards convergence. The similarity in the secondary droplet distributions of both simulations coupled with the ability to accurately predict the splashed mass ratio[12] suggests a resolution of 80 CPD is sufficient to capture secondary droplet formation.

Time Averaged Secondary Droplet Characterization

We will now present the time averaged secondary droplet distributions for all three droplet train impingements. The results are averaged for the impingement of 11 drops, at which point pseudo-steady state impingement dynamics are present, following the conclusion of the transient film formation period. In each simulation the first impinging drop is deposited with no splashing, therefore the results represent the splashing of 10 drops. Due to the difference in impingement frequency each simulation has a different physical end time (longer for higher u), but all results have a similar dimensionless end time (T) which

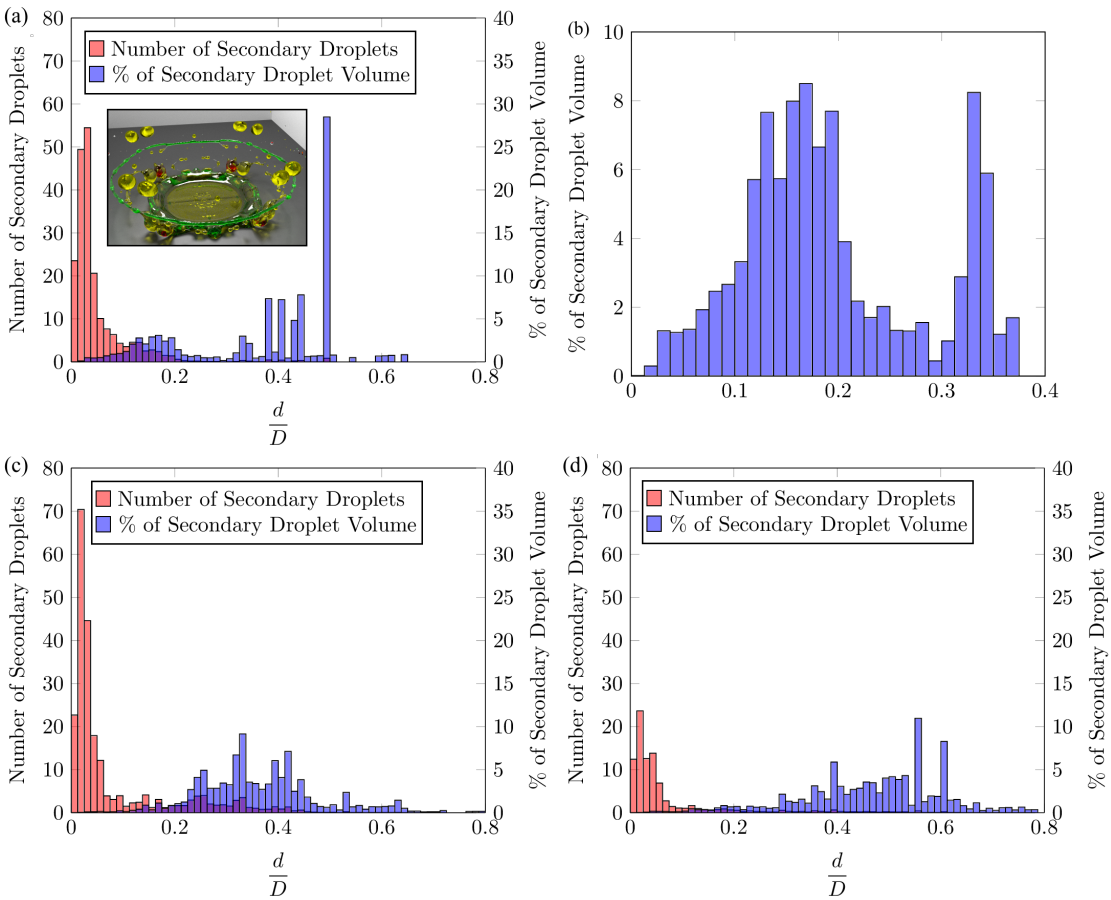

Figure 10. Time averaged number of secondary droplets and percent of secondary droplet volume as a function of d/D for (a) u = 19, with the inlay showing the large secondary droplets responsible for the peak in the percent of secondary droplet volume at d/D = 0.49, (b) percent of secondary droplet volume at u = 19, excluding the large secondary droplets seen in (a), (c) u = 22, and (d) u = 25.

ensures the secondary droplets from the tenth splashing drop are captured. The time averaged secondary droplet characterization results for the impingements at u = 19, 22 and 25 are shown in Figure 10(a), (c) and (d), respectively. Again, the bin size is Δx, or, D/80. Comparing the time averaged secondary droplet distributions, the number of ejected secondary droplets increases as the dimensionless velocity increases, until the impingement at u = 25. At u = 25, the relatively long time between subsequent drop impingements allows the film to recede and strongly interact with the impinging drop, producing a lesser number of smaller droplets compared to the other two cases. This also alters the time averaged droplet number calculation since there are times when most secondary droplets have left the domain before the splashing of the next drop, thus reducing the time averaged number of droplets. Consistent with the instantaneous secondary droplet distributions shown in Figure 6, the largest number of droplets are within d/D = 0.0063-0.056 for all simulations, but this droplet size has a negligible contribution to the volume of secondary droplets. In the Lagrangian-Eulerian simulations using a SWI model, the evaporation time and fuel air mixing are generally quantities of interest. Such quantities may not be accurately predicted if one solely relies on the number of secondary droplets. Therefore, the percent of secondary droplet volume may be used in an improved SWI sub-model to intelligently select the most dominant secondary droplet sizes.

Also consistent with the results of Yarin and Weiss[11], there are a greater number of larger droplets as u increases. At u = 19, there are large peaks in the percent of secondary droplet volume at d/D = 0.38-0.49, seen in Figure 10(a). These large peaks are due to eight large secondary droplets, seen in Figure 10(a) and Figure 4(a), which eventually coalesce into four large droplets. These drops move very slowly, residing in the domain until the impingement of the seventh drop. The small velocity of these droplets is discussed later in Figure 12(a). If the mass of these slowly moving, large secondary droplets, not representative of the majority of impingements, is excluded, then the distribution in the percent of secondary droplet volume, as shown in Figure 10(b), becomes more clear. Now, at u = 19, the majority of the secondary droplet volume is composed of droplets of size d/D = 0.1-0.2, with a second peak at 0.35. The peak at d/D = 0.35 is due to the intact lamella rim before it fractures, the same phenomenon explained in the temporal evolution of secondary droplets for the impingement at u = 22 (Figure 6). As seen in Figure 10(c) at u = 22, the majority of the secondary droplet volume is represented by droplets of size d/D = 0.2-0.425. That shifts to d/D = 0.3-0.6 when the nondimensional velocity is increased to u = 25, shown in Figure 10(d). Similar secondary droplet results at comparable nondimensional velocities were presented in Yarin and Weiss[11]. The same trends in secondary droplet characterizations are seen in the current study as in Yarin and Weiss[11]; however, no direct comparisons are made due to the difference in the analysis domains. The analysis domain in the current study is centered at the impingement point, capturing the secondary droplets formed at short length ($<$ 0.24mm) and temporal (3μs) scales at the

moment of impingement. In Yarin and Weiss[11], however, the sample volume was located 1mm from the impingement point and the results were extrapolated to determine the total ejected droplets from the impingement.

The secondary droplet distributions presented in Figure 10 were modified to show the probability density functions (PDFs) of secondary droplet diameter in Figure 11. Additionally, the PDF from the simulation results are compared to the PDF proposed by Stanton and Rutland[16], which is based on the nondimensional velocity (u) proposed by Yarin and Weiss[11]. In Figure 11, the similarity in the PDFs for all three simulations is apparent, favoring smaller secondary droplets of size d/D = 0.01875. Comparing the results to the model of Stanton and Rutland[16], it is clear the model tends toward larger secondary droplets, predicting most droplets will be of size d/D = 0.1658. Furthermore, the simulation results show the secondary droplet distributions are dependent on the impingement frequency. That dependence is absent in the model of Stanton and Rutland[16]. This analysis suggests improvements can be made to the secondary droplet size predictions in current SWI sub-models through the use of highly resolved simulations such as the ones presented in the current work.

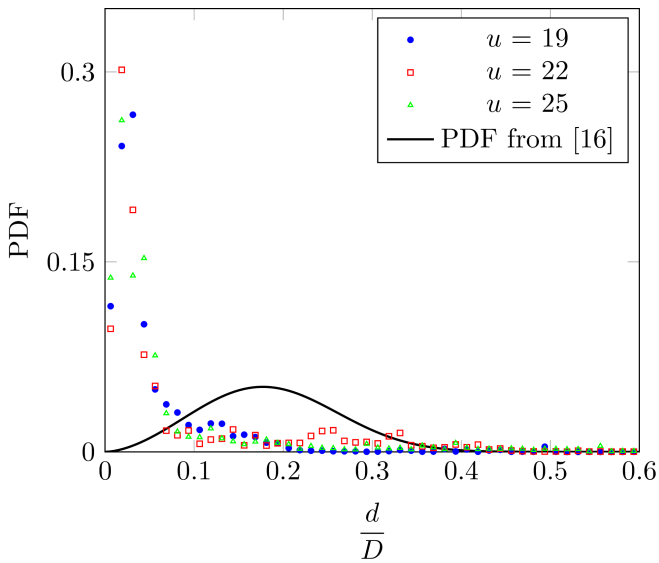

Figure 11. Probability density functions of secondary droplet diameter for the ethanol drop train simulations at u = 19, 22 and 25 compared to the prediction from the model of Stanton and Rutland[16]. The bin size is equal to the grid size (1.375 μm).

Velocity Characterization of Secondary Droplets

The secondary droplet velocities were also characterized to obtain the maximum and time averaged velocity magnitude, which are presented in Figure 12(a-c) for the simulations at u = 19, 22 and 25,

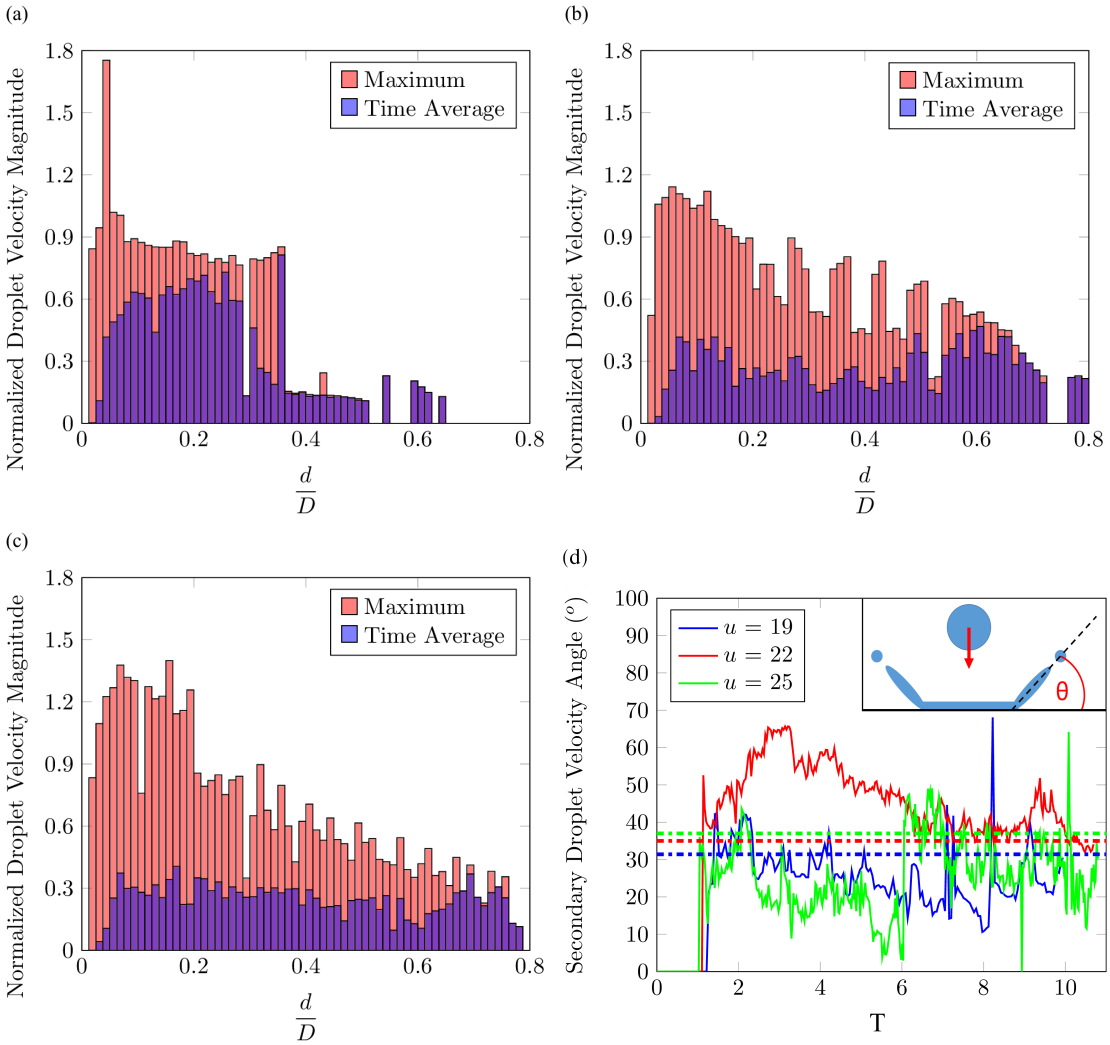

Figure 12. Maximum and time averaged normalized secondary droplet velocities, defined as $|\vec{U}|/V_0$, where V_0 is 10 m/s, as a function of dimensionless diameter for (a) u = 19 (b) u = 22 (c) u = 25. (d) Average velocity angle with respect to horizontal of all secondary droplets as a function of dimensionless time. The dotted lines correspond to the predictions from Fredorchenko and Wang's[28] model for each case.

respectively. In Figures 12(b) and (c), we see very similar trends for both the maximum and time averaged velocity at u = 22 and 25. In both cases the maximum velocity decreases with increasing droplet size. The maximum velocity of any droplet is approximately $1.1V_0$ and $1.4V_0$ for u = 22 and 25, respectively. In both cases, the average velocity is fairly independent of droplet size and is approximately $0.33V_0$. The secondary droplet velocities at u = 19, shown in Figure 12(a), do not follow the same trend; the maximum velocity is constant at approximately $0.9V_0$, excluding the large outlying peak near $1.8V_0$, and the average velocity is constant at about $0.6V_0$, until sharply dropping to $0.2V_0$ at d/D = 0.38. From d/D = 0.39 and greater, the droplet velocity is approximately $0.2V_0$. This velocity is associated with the large secondary droplets (Figure 10(a), inlay) formed during the second drop impingement, as described above.

In Figure 12(d) the average velocity angle with respect to the surface (θ) of all secondary droplets is reported as a function of dimensionless time. At u = 19 and 25, a similar trend is seen, but the velocity angle is less than that of u = 22. The fluctuations in velocity angle during the transient film formation period may be attributed to strong interactions with the developing film. At u = 25, with sufficient time for the film to recede, the impinging drop strongly interacts with the liquid film causing huge variation in velocity angle. Once the film has formed and pseudo-steady state dynamics are present (after the impingement of the seventh drop T $>$ 6), the film thickness for all simulations is approximately 4.0-5.5μm. As previously shown with instantaneous secondary droplet distributions, during the pseudo-steady state impingement regime there is still the possibility for variation of local quantities due to the film shape and momentum at the time of impingement. This leads to the large range of velocity angle seen in Figure 12(d). This effect is also highly dependent on the instantaneous secondary droplet distribution. At certain times during the impingement there may be droplets with a velocity which may not be representative of the majority of secondary droplets formed during splashing. As secondary droplets interact and coalesce, their velocity may deviate from the expected value. When the number of droplets in the domain becomes small, it is possible for such droplets to dominate the average velocity angle, further contributing to the variation of secondary droplets seen in Figure 12(d). Once pseudo-steady state impingement dynamics are achieved, the velocity angle becomes more consistent and is in the 25-40^o range, which can be compared with the findings of Fredorchenko and Wang [28]. In their work an expression for crown angle was derived as Cosθ = 1 - 4H*, where H* = h/D is the dimensionless film thickness and h is the film thickness. Their model predicts a crown angle between 31.4^o and 37^o for our simulations, at the pseudo-steady state (T $>$ 6). Comparing this result with Figure 12(d), the secondary droplet velocity angles in this phase are in fair agreement with the model of Fredorchenko and Wang [28]. The velocity angle for both u = 19 and 25 simulations are slightly below the predicted values, while the velocity angle from the u = 22 simulation is slightly above the predicted value when compared to the model of Fredorchenko and Wang [28].

Summary and Conclusions

In this work, an in-house 3D multiphase flow solver was used to perform highly resolved simulations of the impingement of a train of ethanol drops onto a solid surface at various impingement frequencies, following the experiments of Yarin and Weiss [11]. With the use of a passive scalar routine, each drop within the drop train was individually tagged and tracked throughout the impingement process. This provided a unique view of the splashing process unobtainable through experiments. With the ability to resolve such small length and temporal scales and the use of passive scalars, a unique analysis of the drop train impingement process was possible. A robust secondary droplet characterization algorithm was developed, which scrutinizes the liquid volume field, identifies individual droplets, and characterizes their properties. Using the secondary droplet characterization algorithm, the temporal evolution of the secondary droplet distribution was presented, highlighting the distinct droplet formation phases. Time averaged secondary droplet numbers, percent of total secondary droplet volume and velocities were reported as a function of droplet size for each scenario. The probability density functions of secondary droplets were compared with model proposed by Stanton and Rutland [16], demonstrating a dependence on impingement frequency which is absent in that model. The secondary droplet velocity angle with respect to the surface was also characterized, showing good agreement with an empirical crown angle model [28]. It was shown that highly resolved numerical simulations and unique computational tools can provide detailed insight into the multidrop impingement phenomena. Datasets similar to the ones presented in the current study are necessary to develop physics-based SWI models, which are needed to improve the predictive capability of fuel spray impingement simulations performed in Lagrangian solvers.

Funding

This material is based upon work supported by the Department of Energy, Office of Energy Efficiency and Renewable Energy (EERE) and the Department of Defense, Tank and Automotive Research, Development, and Engineering Center (TARDEC), under Award Number [DE-EE007292] and the Massachusetts Clean Energy Center. The computations were performed on the HPC cluster of the UMass-Dartmouth's Center for Scientific Computing and Visualization Research supported by the ONR DURIP grant N00014-18-1-2255 "A Heterogeneous Terascale Computing Cluster for the Development and Efficient Implementation of High-Order Numerical Methods" and on MGHPCC.

References

1. Borthwick P R and Farrell V P. Fuel Injection Spray and Combustion Chamber Wall Impingement in Large Bore Diesel Engines. *SAE Technical Paper 2002-01-0496* 2002; .

2. Lee SY, Turns S and Santoro R. Measurements of soot, OH, and PAH concentrations in turbulent ethylene/air jet flames. *Combustion and Flame* 2009; 156: 2264–2275.
3. Moreira A, Moita A and Panão M. Advances and challenges in explaining fuel spray impingement: How much of single droplet impact research is useful? *Progress in Energy and Combustion* 2010; 36: 554–580.
4. Yarin A. Drop Impact Dynamics: Splashing, Spreading, Receding, Bouncing. *Annual Review of Fluid Mechanics* 2006; 38: 159–192.
5. Liang G and Mudawar I. Review of mass and momentum interactions during drop impact on a liquid film. *International Journal of Heat and Mass Transfer* 2016; 101: 577–599.
6. Bai C, Rusche C and Gosman A. Modeling of Gasoline Spray Impingement. *Atomization and Sprays* 2002; 12: 1–28.
7. Mundo C, Sommerfield M and Tropea C. On the Modeling of Liquid Sprays Impinging on Surfaces. *Atomization and Sprays* 1998; 8: 625–652.
8. O'Rourke P and Amsden A. A Spray/Wall Interaction Submodel for the KIVA-3 Wall Film Model. *SAE Technical Paper 2000-01-0271* 2000; .
9. Roisman, Horvat and Tropea. Spray impact: Rim transverse instability initiating fingering and splash, and description of a secondary spray. *Physics of Fluids* 2006; 18(10): 102104–102104–19.
10. Markt Jr D, Torelli R, Pathak A et al. Using a DNS Framework to Test a Splashed Mass Sub-Model for Lagrangian Spray Simulations. *SAE Technical Paper 2018-01-0297* 2018; .
11. Yarin A and Weiss D. Impact of drops on solid surfaces: self-similar capillary waves, and splashing as a new type of kinematic discontinuity. *Journal of Fluid Mechanics* 1995; 283: 141–173.
12. Markt Jr D, Pathak A and Raessi M. Advanced Computational Simulations of Surface Impingement of a Train of Ethanol Drops: Pathway to Developing Spray-Wall Interaction Submodels. *Computing in Science and Engineering* 2018; 20(4): 58–65.
13. Mundo C, Sommerfield M and Tropea C. Droplet-Wall Collisions: Experimental Studies of the Deformation and Breakup Process. *International Journal of Multiphase Flow* 1995; 21(2): 151–173.
14. Samenfink W, Elsäßer A, Dullenkopf K et al. Droplet interaction with shear-driven liquid films: analysis of deposition and secondary droplet characteristics. *International Journal of Heat and Fluid Flow* 1999; 20: 462–469.
15. Richter B, Dullenkopf K and Bauer H. Investigation of secondary droplet characteristics produced during wall impact. *12th International Symposium on Applications of Laser Techniques to Fluid Mechanics* 2004; .
16. Stanton and Rutland. Modeling Fuel Film Formation and Wall Interaction in Diesel Engines. *SAE Technical Paper 960628* 1996; .
17. Cossali G, Marengo M and Santini M. Impact of single and multiple drop arrays on a liquid film. *12th International Symposium on Applications of Laser Techniques to Fluid Mechanics* 2004; .

18. Sivakumar D and Tropea C. Splashing Impact of a Spray onto a Liquid Film. *Physics of Fluids* 2002; 14(12): L85–L88.
19. Roisman and Tropea. Fluctuating flow in a liquid layer and secondary spray created by an impacting spray. *International Journal of Multiphase Flow* 2005; 31: 179–200.
20. Pathak A and Raessi M. A 3D, fully Eulerian, VOF-based solver to study the interaction between two fluids and moving rigid bodies using the fictitious domain method. *Journal of Computational Physics* 2016; 311: 87–113.
21. Pathak A and Raessi M. A three-dimensional volume-of-fluid method for reconstructing and advecting three-material interfaces forming contact lines. *Journal of Computational Physics* 2016; 307: 550–573.
22. Youngs D. An Interface Tracking Method for a 3D Eulerian Hydrodynamics Code. *Atomic Weapons Research Establishment (AWRE) Technical Report 44/92* 1984; .
23. Chorin A. Numerical Solution of the Navier-Stokes Equations. *Mathematics of computation* 1968; 22(104): 745–762.
24. Rudman M. A Volume-Tracking Method for Incompressible Multifluid Flows with Large Density Variations. *International Journal of Numerical Methods in Fluids* 1998; 28(2): 357–378.
25. Francois M, Cummins S, Dendy E et al. A balanced-force algorithm for continuous and sharp interfacial surface tension models within a volume tracking framework. *International Journal of Heat and Fluid Flow* 2006; 213(1): 141–173.
26. Freniere C, Pathak A, Raessi M et al. The Feasibility of Amazon's Cloud Computing Platform for Parallel, GPU-Accelerated, Multiphase-Flow Simulations. *Computing in Science and Engineering* 2016; 18(5): 68–77.
27. Pathak A, Freniere C and Raessi M. Advanced computational simulations of water waves interacting with wave energy converters. *European Journal of Computational Mechanics* 2017; 26: 172–204.
28. Fredorchenko A and Wang A. On some common features of drop impact on liquid surfaces. *Physics of Fluids* 2004; 16(5): 1349–1365.